ADVANCED MATERIALS
www.advmat.de

Upcycling of Waste Plastic into Hybrid Carbon Nanomaterials

Kevin M. Wyss, John T. Li, Paul A. Advincula, Ksenia V. Bets, Weiyin Chen, Lucas Eddy, Karla J. Silva, Jacob L. Beckham, Jinhang Chen, Wei Meng, Bing Deng, Satish Nagarajaiah, Boris I. Yakobson,* and James M. Tour**

Graphitic 1D and hybrid nanomaterials represent a powerful solution in composite and electronic applications due to exceptional properties, but large-scale synthesis of hybrid materials has yet to be realized. Here, a rapid, scalable method to produce graphitic 1D materials from polymers using flash Joule heating (FJH) is reported. This avoids lengthy chemical vapor deposition and uses no solvent or water. The flash 1D materials (F1DM), synthesized using a variety of earth-abundant catalysts, have controllable diameters and morphologies by parameter tuning. Furthermore, the process can be modified to form hybrid materials, with F1DM bonded to turbostratic graphene. In nanocomposites, F1DM outperform commercially available carbon nanotubes. Compared to current 1D material synthetic strategies using life cycle assessment, FJH synthesis represents an 86–92% decrease in cumulative energy demand and 92–94% decrease in global-warming potential. This work suggests that FJH affords a cost-effective and sustainable route to upcycle waste plastic into valuable 1D and hybrid nanomaterials.

1. Introduction

1D carbon materials have received substantial research and attention since their discovery in the late 20th century.[1–4] Although carbon nanotubes present the most widely acknowledged example of such 1D materials, many subclasses, and different morphologies have been characterized.[5,6] Examples of these 1D carbon nanomaterials include carbon nanotubes (CNTs), both single- and multi-walled, as well as ribbon- and plate-like carbon nanofibers, bamboo-like carbon nanotubes, cup-stacked carbon nanofibers, and many more.[7–10] 1D materials are used extensively in composites, coatings, sensors, electrochemical energy storage, and electrocatalysts, capitalizing upon their strength, conductivity, low density, broadband electromagnetic absorption, high surface area, and chemical robustness.[11–14] Due to their broad utility and scientific interest, identifying new methods of synthesizing 1D carbon materials remains critical. The majority of synthetic strategies to form 1D carbon materials, including arc-discharge, laser ablation, chemical vapor deposition, plasma torch, and high partial pressure carbon monoxide involve the mobilization of carbon atoms in feedstocks on the surface of a catalytic metal which then grow into a graphitic 1D morphology.[15] These current methods often result in mixtures of 1D materials and amorphous carbon that require separation, and 1D materials syntheses often suffer from low production rates of <1 g h^{-1}.[16–18]

Some recent work has focused on converting waste plastic into higher value carbon nanomaterials, inspired by the low

---

K. M. Wyss, J. T. Li, P. A. Advincula, W. Chen, L. Eddy, K. J. Silva,
J. L. Beckham, J. Chen, B. Deng, B. I. Yakobson, J. M. Tour
Department of Chemistry
Rice University
6100 Main Street, Houston, TX 77005, USA
E-mail: biy@rice.edu; tour@rice.edu

K. V. Bets, S. Nagarajaiah, B. I. Yakobson, J. M. Tour
Department of Materials Science and NanoEngineering
Rice University
6100 Main Street, Houston, TX 77005, USA
E-mail: satish.nagarajaiah@rice.edu

L. Eddy
Applied Physics Graduate Program
Rice University
6100 Main Street, Houston, TX 77005, USA

W. Meng, S. Nagarajaiah
Department of Civil and Environmental Engineering
Rice University
6100 Main Street, Houston, TX 77005, USA

S. Nagarajaiah
Department of Mechanical Engineering
Rice University
6100 Main Street, Houston, TX 77005, USA

S. Nagarajaiah, B. I. Yakobson, J. M. Tour
Welch Institute for Advanced Materials
Rice University
6100 Main Street, Houston, TX 77005, USA

B. I. Yakobson, J. M. Tour
Smalley-Curl Institute, NanoCarbon Center
Rice University
6100 Main Street, Houston, TX 77005, USA

The ORCID identification number(s) for the author(s) of this article can be found under https://doi.org/10.1002/adma.202209621.

DOI: 10.1002/adma.202209621

cost and high availability of the feedstock.[19–21] However, these methods often use a two-step chemical vapor deposition pyrolysis process: the first stage deconstructs the plastic into volatile hydrocarbons under an inert atmosphere at temperatures of 700–900 °C for 0.5–2 h.[22,23] In the second stage, the hydrocarbon gases then grow into 1D materials on complex transition metal catalysts, once again under inert atmosphere at similarly high temperatures for multiple hours.[24–26] The growth catalysts generally require dedicated synthesis or templating methods that can be time, energy, and resource intensive.[27–29] Further, many of these methods use 1:1 ratios of waste plastic to growth metal complex, meaning that every 1 ton of waste plastic processed would require 1 ton of metal complex to be manufactured, which would hamper widespread implementation and economic viability.[30] To our knowledge, the production of complex carbon hybrid nanomaterials from waste plastic has not been demonstrated. Current methods of carbon nanomaterial production from waste plastic are hampered by long reaction durations and high resource consumption, large amounts of metal complex additive, and minimal scalability of chemical vapor deposition techniques.

Flash Joule heating (FJH) was recently leveraged as efficient methods for the solvent-free synthesis of a variety of carbonaceous and inorganic nanomaterials.[31–35] Particularly, FJH has presented a facile method to upcycle low-value waste materials into high-value nanomaterials.[36–39] For the FJH synthesis of graphene, electrical energy and resistance are leveraged to rapidly generate high temperatures and form turbostratic, or rotationally mismatched, graphene as the short duration of FJH (0.05 to 0.5 s) limits the rotational movement. Temperatures >3100 K are accessed in milliseconds, allowing for the reorganization of amorphous carbon bonding into highly ordered sp^2-hybridized sheets.[32] Flash graphene sheets form through a "mobile carbon" mechanism, with temperatures generated by high resistance junctions within the sample allowing for annealing and formation of crystallized nanoparticles.[40] The capacitance density of the reaction can also control reaction conditions; increasing charge per unit mass shifts the nucleation process from reaction limited to diffusion-controlled reaction kinetics.[36,41]

To our knowledge, FJH has not yet been leveraged in 1D materials synthesis. Given that graphitic 1D nanomaterials are grown through the deposition of mobile carbon on metallic nanoparticles, and that FJH can efficiently and rapidly produce mobile carbon, we were inspired to study the growth of carbon 1D nanomaterials using FJH. Here, we demonstrate the conversion of plastic into 1D materials and hybrid graphitic 1D/2D materials, with controllable morphologies. The process utilizes in situ catalysis and enables directional control over the assembly of mobile carbon during FJH, advancing our understanding of the technique. The produced flash 1D materials (F1DM) demonstrate excellent mechanical behavior in vinyl ester composites, attributable to the hybrid morphology and indicative of the value and utility of the waste plastic upcycled product. Further, FJH presents substantial advantages over classical 1D synthesis when analyzed using a cradle-to-gate perspective life cycle assessment.

2. Results and Discussion

2.1. Synthesis of F1DM

FJH was recently identified as an efficient method for the solvent-free synthesis of carbonaceous and inorganic nanomaterials, in which electrical energy and resistance are leveraged to rapidly (0.05–3 s) generate high temperatures (≈3000 K), allowing for the solvent-free upcycling of low-value waste materials into high-value products.[31,33,42] Graphitic 1D and hybrid nanomaterials often grow through the deposition of mobile carbon on metallic nanoparticles, and FJH is known to efficiently produce mobile carbon, inspiring the study of the growth of 1D nanomaterials using FJH. Introducing low concentrations of simple, earth-abundant transition metal salts into the carbonaceous polymer feedstock results in graphitic 1D material growth, catalyzed in situ during the FJH process (**Figure 1**a).[36,40] Iron(III) chloride, nickel(II) chloride, cobalt(II) chloride, and ferrocene were used as the growth catalysts. A polymer feedstock was selected due to the abundance and low cost of waste plastic and the resulting yield of F1DM. The resistance of the reaction mixture is easily controlled by adjusting the amount of conductive carbon additive such as carbon black or metallurgical coke.[33,43] The high resistance of a plastic precursor allows for many high-resistance junctions between particles in the sample, resulting in high overall and local temperatures. Further discussion of the FJH parameters and system is provided in the Experimental Section and Figures S1 and S2, Supporting Information.

The polymer feedstock was loaded with catalyst particles through surface wetting or melt mixing. For surface wetting, the polymer was sonicated in an aqueous alcohol solution containing 0.1 g mL^{-1} of salt, then filtered and dried to coat the surface of the polymer with small amounts of the catalyst. For solvent-free catalyst loading, melt-mixing can be used wherein metal complexes such as ferrocene and polymers with similar melting points are mixed mechanically in the melt state and no solvent is used. Scanning electron microscopy (SEM) images (Figure 1a–c) show fibers of varying diameters are formed during the FJH process. A typical aspect ratio of 330 was observed (Figure S3a–f, Supporting Information) but often the entire intertwined length could not be continuously tracked so this is likely an underestimate.

Quantitatively differentiating between graphitic carbon morphologies is a difficult task, as 1D and 2D morphologies look almost identical by common analytical methodologies such as X-ray photoelectron spectroscopy (XPS) and thermogravimetric analysis (TGA), with Raman and powder X-ray diffraction (XRD) showing only minor differences. These techniques are discussed and contrasted in the following section, but due to the combination of morphologies obtained during FJH, extensive SEM imaging was used to determine the morphological share of each sample. At low magnifications, 1D and 2D morphologies can look similar (Figure S4, Supporting Information), so for each sample, 108 different images over 9 different areas are examined and assigned a dominant morphology (1D, 2D, or hybrid). This allows for the morphological percentage, in area%, to be quantitatively determined. Area% is used throughout the rest of the manuscript when discussing F1DM morphology

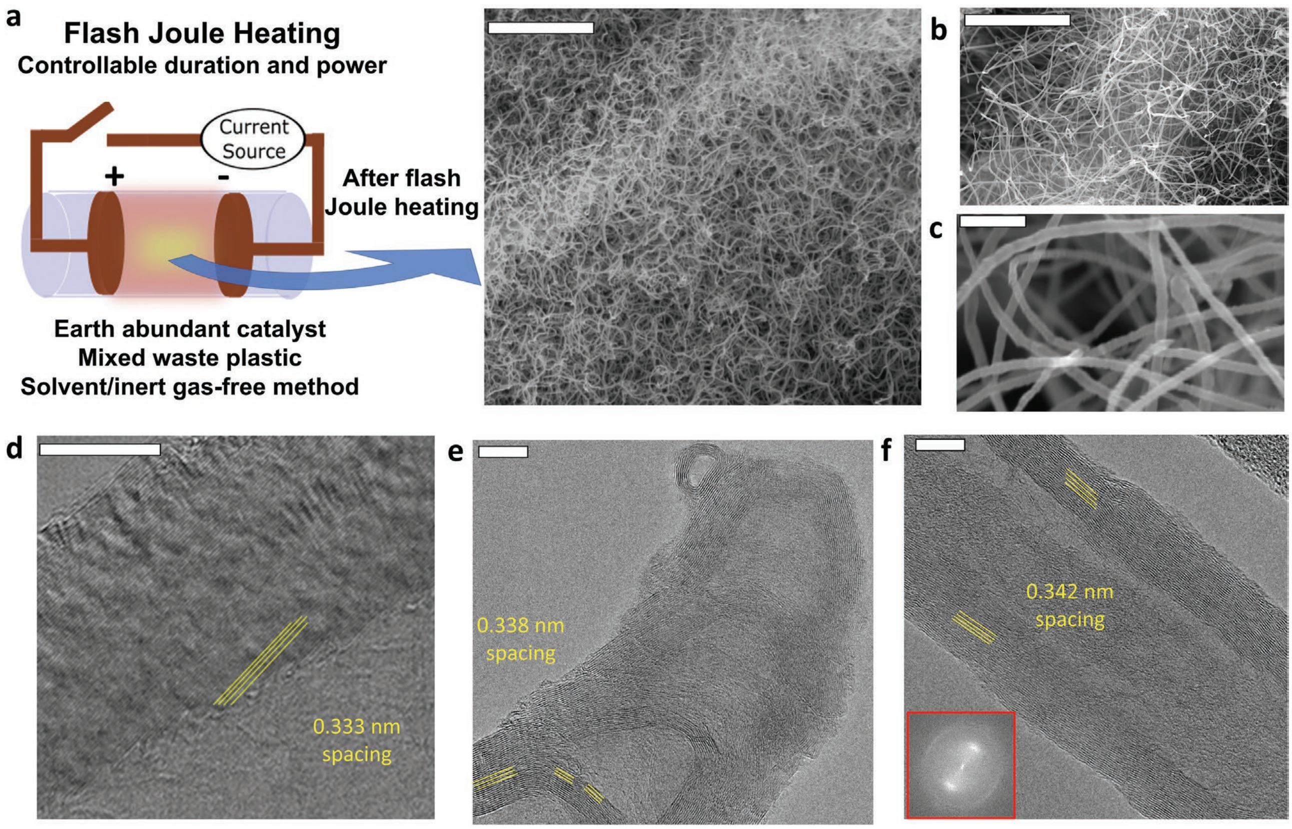

Figure 1. Preparation of F1DM. a) Schematic of FJH process forming F1DM with a representative SEM image showing carbon F1DM-rich area of the sample. b,c) SEM images of F1DM rich areas within the sample, showing the tangled arrangement of 1D materials produced. d–f) TEM images of different F1DM morphologies including: d) ribbon-type nanofiber, e) bamboo-like nanofiber, and f) multi-walled nanotubes. Lattice fringes are highlighted with yellow lines to help guide the eye, and the average interlayer spacing for each morphology is also provided. The fast Fourier transform of (f) is shown in the inset demonstrating the prominent (002) fringe of the nanotube. The scale bars in the images correspond to: a) 5 µm, b) 3 µm, c) 300 nm, d–f) 10 nm.

yield. A maximum of ≈65% of the solid product is 1D morphology with the remainder composed of 2D turbostratic graphene (Figure S4, Supporting Information). Figure 1d–f shows high resolution TEM images of ribbon-like carbon nanofibers, graphitic bamboo-like carbon, and multi-walled carbon nanotubes. Bamboo-like carbon nanofibers with many layers stacking in a cup-like manner comprise the dominant F1DM morphology. The 2D morphologies present can be observed by TEM imaging (Figure S5, Supporting Information). Graphene nanoribbons can also be observed through TEM imaging which could result from the high-temperature unzipping of carbon nanotubes (Figure S6, Supporting Information).[44,45]

2.2. Characterization of F1DM

F1DM were characterized using Raman spectral mapping, which demonstrates highly graphitic character over a large area (Figure S7, Supporting Information).[39,41] The F1DM was compared to a control sample, where no metal was included but all other conditions were identical and both samples yielded products with 97–98% graphitic character. The graphitic character can be determined by three different characterization methods including Raman spectroscopy, TGA, and high-resolution XPS. Wide-area Raman mapping was carried out by collecting 100 unique spectra, over a 4 mm^2 area, which are then processed using MatLab scripts which characterize spectra with a I2D/IG ratio >0.3 to be graphitic. TGA can be used to determine graphitization by measuring the thermally stable mass at 550 °C under an air atmosphere, since amorphous carbon will degrade below this temperature. High-resolution XPS and fitting of the C1s peak can allow for graphitic character to be determined, and a more accurate method of C KLL XPS (detailed in Figure S10, Supporting Information) can also probe graphitic content. High resolution, extended exposure Raman spectroscopy reveals the presence of radial breathing mode peaks in the F1DM sample indicating the presence of carbon nanotubes in the F1DM sample, but not in the metal-free control sample (**Figure 2**a,b). By varying the Raman excitation wavelength, different radial breathing mode peaks can be observed (Figures S8 and S9, Supporting Information). The low intensity M, TS$_1$, and TS$_2$ peaks can also be observed (Figure 2c). The M peak, located at 1750 cm^{-1}, indicates ordered AB stacking.[46] The TS$_1$ and TS$_2$ peaks, located at 1875 cm^{-1} and 2050 cm^{-1}, respectively, indicate disordered turbostratic stacking.[47,48] The presence of both the M and TS peaks indicate that both aligned and misaligned stacking of graphitic domains are present. Flash graphene is turbostratic, so M peak presence was unexpected.[31,32]

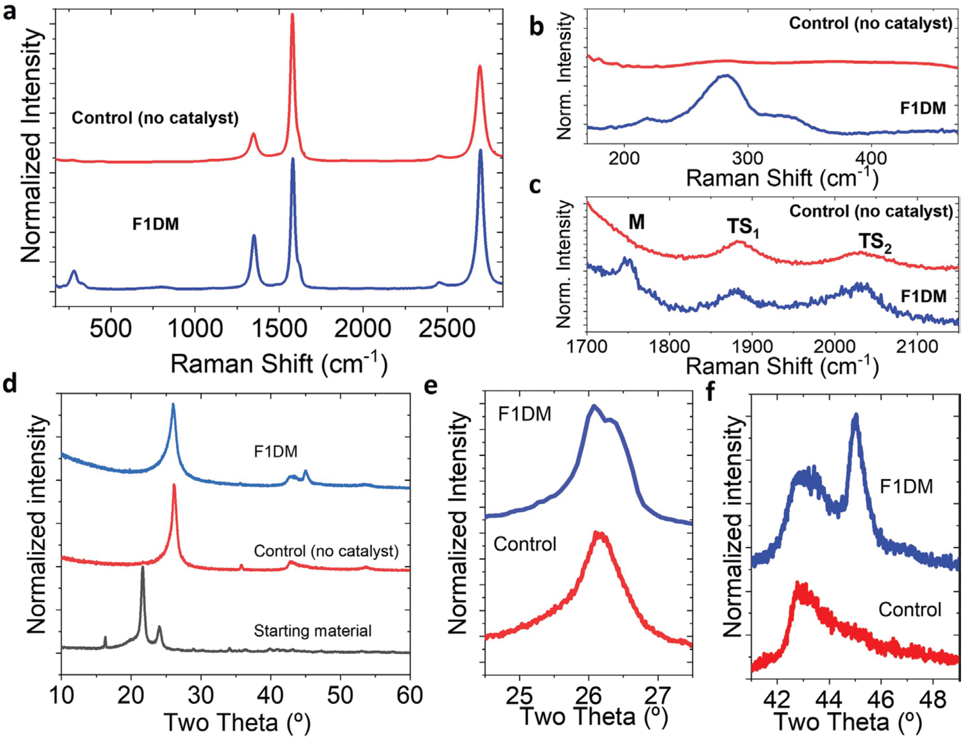

Figure 2. Characterization of F1DM. a) A representative high resolution extended Raman spectrum of a sample of F1DM compared to a control sample where no metal was incorporated but all FJH parameters were the same. b) Raman spectra comparing the F1DM sample to the control sample, showing the average Raman spectra from a 36 µm^2 area and the absence of radial breathing mode peaks in the control sample. c) Raman spectra comparing the M, TS$_1$, and TS$_2$ peaks in the high-resolution F1DM sample to the control sample, showing the presence of the M peak only in the F1DM sample. d) Powder XRD comparing the F1DM to the starting material and a control sample where no metal catalyst was used, but all other parameters are identical. e) Powder XRD spectra comparing the (002) peak of the F1DM and control sample, showing the multi-Lorentzian peak of the F1DM. f) Powder XRD spectra showing the (101) and (100) peak area, showing the enhanced (101) peak in the F1DM sample.

Catalytically synthesized plate- and ribbon-like carbon nanofibers often demonstrate rotationally ordered AB stacking, which might explain the presence of the M peak and further indicate the bulk presence of nanofiber morphologies in F1DM.[49,50]

To characterize the bulk F1DM product, powder XRD was used (Figure 2d), showing a broad, intense, and multi-Lorentzian (002) peak indicating graphitic structure. The F1DM (002) peak is fit by two distinct Lorentzians, occurring at 26.46° and 26.11° (Figure 2e). The (002) peak of the catalyst-free control sample is fit with a single Lorentzian centered at 26.12°. Graphitic 1D materials, such as MWCNT and CNF have nearly identical diffractograms to that of 2D graphene because they share the same unit cell. The only difference is the interlayer spacing of turbostratic graphene (0.35 nm) as compared to that of graphitic 1D materials (0.34 nm), reflected by the position of the (002) peak. A lattice spacing of 0.350 nm corresponds to a diffraction peak of 26.1°, while a decreased lattice spacing would result in shifting the diffraction peak to higher angles. The fitting of the F1DM (002) peak by two distinct Lorentzian functions indicates that both 1D materials and turbostratic graphene are present in the sample, whereas the single peak in the control sample corresponds only to turbostratic graphene. It is also known that the position of the (002) peak is dependent on the diameter of the carbon nanotube or nanofiber, and (002) peaks that can be fit by multiple sub-peaks.[51] Further, an enhanced (101) peak at 45.3° can be observed in the F1DM, but not in the catalyst-free control sample (Figure 2f), as observable for large diameter carbon nanotubes.[51]

XPS was used to probe the elemental content and bonding of F1DM (Figure S10a, Supporting Information). During FJH, the high boiling point of carbon results inthe plastic being enriched to a 97.8% graphitic product. High resolution spectra of the C1s transition demonstrate minimal oxygen content and the π–π* transition, located at 291 eV (Figure S10b, Supporting Information). The D-parameter of the starting material polymer is 12.8 eV, which increases to 20.2 eV after FJH, signifying a transition from sp^3- to sp^2-hybridization (Figure S10c, Supporting Information). Thermogravimetric analysis of F1DM under air atmosphere shows high degradation onset temperature of 630 °C, confirming the bulk graphitic character (Figure S11a, Supporting Information).

The limit of detection for XPS survey scans is typically 0.5 to 1.0 at%. Thus, at the concentrations determined by ICP-MS, with a maximum of 0.3 wt%, we would not expect to detect any metal catalyst by XPS survey scans. Further, the penetration depth of XPS detection is only 1–2 nanometers. Since TEM imaging shows that the iron is present in nanoparticles below many layers of graphitic carbon, it is also likely that the iron photoelectrons are not detected. In contrast, the iron is solubilized following sample digestion as it is prepared for ICP-MS testing, and ICP-MS has much lower limits of detection. Inductively coupled plasma mass spectrometry reveals that F1DM formed using the surface wetting method of 0.1 g mL^{-1} FeCl$_3$ on a virgin high-density polyethylene (HDPE) feedstock showed only 0.3 wt% Fe content in the starting material, decreasing during FJH to 0.06 wt% (Figure S12, Supporting Information). The reduction in catalyst content during the FJH process is likely due to sublimation and outgassing of the metal ions at high temperatures.[52] The catalyst content can be further reduced to <10 ppm with 1 м HCl wash (Figure S12, Supporting Information).

2.3. F1DM from Untreated, Post-Consumer, Mixed Plastics

There are 27 million tons of mixed waste plastic landfilled annually. Motivated by this, we converted mixed post-consumer waste plastic into F1DM by grinding, surface wetting, and FJH. **Figure 3** shows that mixed waste plastic composed of HDPE, low-density polyethylene (LDPE), polypropylene (PP), polystyrene (PS), and poly(ethylene terephthalate) (PET), can be easily upcycled into F1DM by a 3-s-long FJH pulse. Other recent research described the synthesis of graphitic 1D materials from waste plastic.[21,24,27] However, those methods often relied on two-stage 2-h-long pyrolysis followed by catalyst-aided chemical vapor deposition methods and have not been shown to accommodate mixed waste plastic streams, and can result in mixtures composed of ≈30 wt% amorphous carbon or large excesses of catalyst that must be further removed.[53,54]

The mixed waste plastic mixture used is composed of 42% HDPE, 20% PP, 20% LDPE, 10% PS, 8% PET, replicating the global plastic waste composition. It is known that pyrolysis and

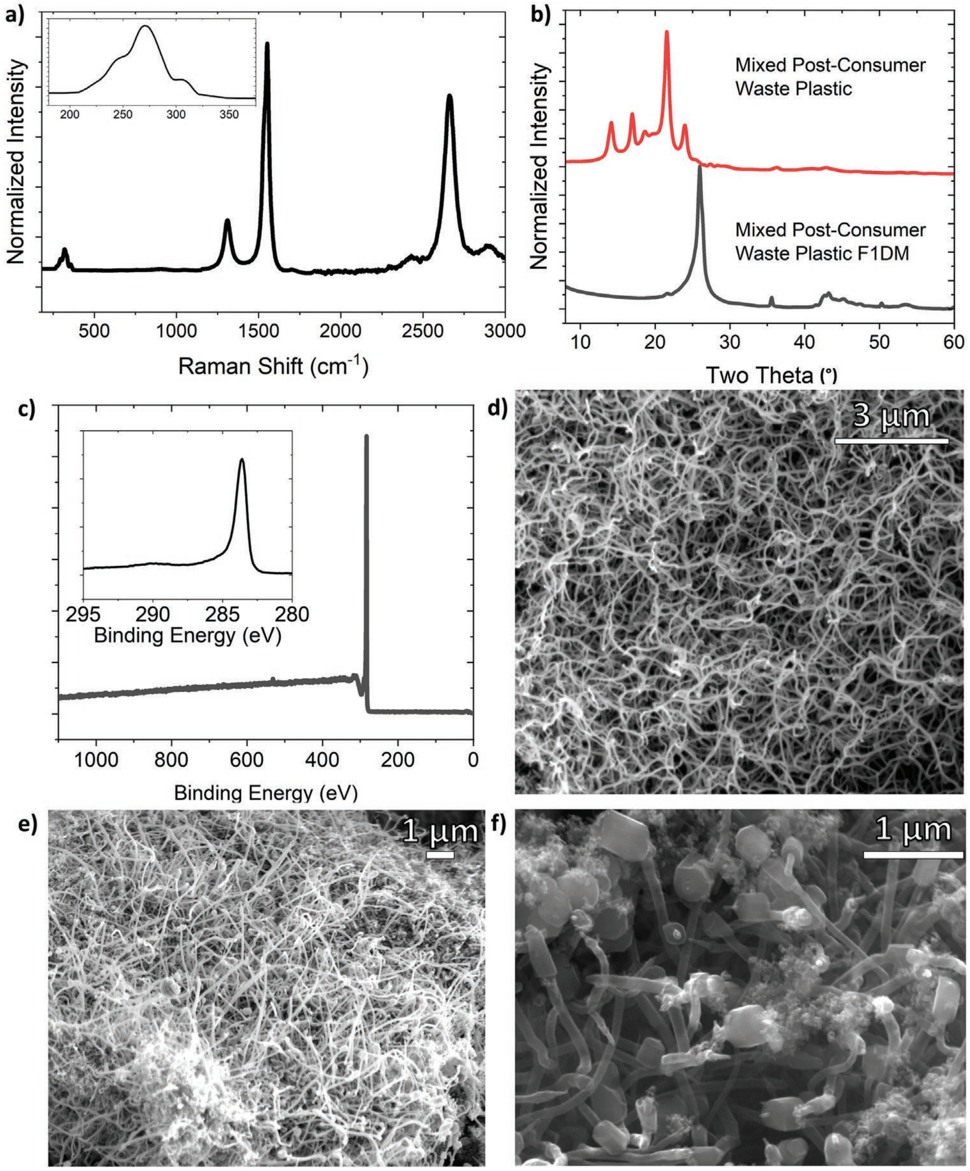

Figure 3. Characterization of F1DM synthesized from post-consumer mixed waste plastic. a–f) Mixed waste plastic derived F1DM characterized by: a) large-area average Raman spectrum with the inset showing the radial breathing modes, b) powder XRD comparing the waste plastic to the synthesized F1DM, c) survey and high-resolution XPS analysis, d–f) SEM images showing morphologies of waste plastic derived F1DM.

FJH of PET result in lower carbon yields, and a lower yield of 1D graphitic materials.[36,55] The conversion of polystyrene was further investigated as some studies have reported that the aromatic structures result in thicker CNTs.[55] This trend was also observed for F1DM (Figure S13a, Supporting Information). Radial breathing modes can be observed for the waste derived F1DM (Figure 3a), as well as complete conversion of the waste plastic into graphitic structures, as determined by powder XRD (Figure 3b) and TGA (Figure S11b, Supporting Information). The enhanced (101) peak can also be observed in Figure 3b, confirming the bulk presence of F1DM synthesized from mixed waste plastic. High elemental purity in the produced F1DM can be further studied by XPS (Figure 3c), which shows a 2% increase in oxygen content as compared to HDPE derived F1DM despite the inclusion of PET, which is 25 wt% oxygen. Additives, such as colorants, plasticizers, adhesives, or residual waste from the plastics' primary use are regarded as impurities. The TGA (Figure S11b, Supporting Information) and XRD (Figure 3b) of the mixed waste plastics do not show substantial metallic impurities, as signified by low residual TGA mass and minimal unidentified XRD peaks. The atomic carbon in these impurities can be converted to graphene while heteroatoms such as oxygen, metals, or halides, are lsublimed out. F1DM morphologies, including hybrid morphologies, can be observed by SEM imaging as shown in Figure 3d–f.

The particle size of the waste polymer feedstock has been demonstrated to impact the results of FJH,[36] and the finer particle size will allow for more catalyst loading and higher surface area of high resistance junctions, improving the yield of F1DM. Thus, the yield of F1DM in the post-consumer polymer samples may be further increased by improved grinding. We ground the mixed waste plastic as fine as our hammer mill allowed, but industrial scaling would afford smaller particles and thus more surface for the F1DM to form. Many types of polymers exist, and high melting temperatures of some may not allow for the catalyst to be introduced by melt-mixing. To demonstrate process generality, polyurethane, a thermoset polymer, was converted into F1DM through a simple surface wetting technique. These F1DM synthesized from waste polyurethane demonstrated similar properties and morphologies as those derived from virgin HDPE (Figure S13b, Supporting Information). Polyurethane derived F1DM did have slight increases in oxygen (2.3%) and nitrogen (1.4%) content, indicating that the formation of heteroatom doped 1D and hybrid morphologies may be possible by FJH, something that has already been demonstrated for FJH graphene.[56]

2.4. Controllable Hybrid and F1DM Morphologies

1D and 2D hybrid materials, such as rebar graphene, are desirable for study and application due to their exotic mechanical and electronic properties.[57,58] However, these materials are almost singularly synthesized through multistep chemical vapor deposition methods that are high-cost and low-yielding.[59,60] FJH produces areas of 2D graphene morphologies, F1DM morphologies, and commonly observable areas of colocalization and coalescence of 1D and 2D morphologies (**Figure** 4a–i). SEM imaging demonstrates F1DM decorated with 2D graphene sheets at their ends, with the 1D morphology occasionally extending all the way through the 2D graphene (Figure 4a,c,d). Areas of the sample (Figure 4b) also exhibit the coalescence of 1D morphologies into larger-diameter 1D materials and then networks of 2D graphitic morphologies.[40] TEM imaging (Figure 4e–i) shows colocalization of F1DM and graphene. High-resolution imaging (Figure 4e–g) shows that the lattice fringe and edge are uninterrupted from the external wall of the nanofiber to the larger graphene sheet, indicating van der Waals interactions connecting the 1D and 2D domains together. Atomic-resolution TEM imaging (Figure 4h) reveals hexagonal sp^2-hybridized graphene sheets, uninterrupted along the edge at the junction between the 1D and 2D morphology, suggesting covalently linked hybrid materials. The fast Fourier transform (Figure 4i) indicates AB-stacked graphene, suggesting that hybrid materials may result in the observed decrease in lattice spacings by XRD and occurance of the M peak in Raman spectral analysis (Figure 2).

We hypothesized that FJH parameters, including discharge voltage, catalyst type, loading, and capacitance density, would impact the product morphologies. Capacitance density is defined here as the system capacitance per unit mass reacted.[41] SEM analysis reveals that catalyst loading and type impact the diameter of the produced F1DM (**Figure 5**a,b) with decreasing catalyst loadings resulting in thinner 1D materials being produced, with Fe(III) producing the thinnest F1DM and Co(II) producing the thickest. It is well known that catalyst type can have substantial impact on the size of produced CNTs, since different metals have different catalytic graphitization rates and carbon solubilities.[61–63] In agreement with the present work, many literature reports suggest that iron is more effective than cobalt and nickel, possibly due to these impacts. FJH parameters such as capacitance density and pulse voltage directly correlate with the capacitive current by Equation (1) and affect the diameter of F1DM (Figure 5c,d), where *I*, *C*, *V*, and *t* correspond to current, capacitance, voltage, and time, respectively.

$$I = C\frac{d(V)}{d(t)} \tag{1}$$

Intriguingly, capacitance and pulse voltage discharge result in opposite trends in F1DM diameter, despite both contributing additional charge to the reaction. However, the discharge rate of a capacitor is not uniform, so doubling the capacitance will not double the current but would instead double the discharge time. The amount of time required for the capacitors to discharge can be determined by using Equation (2), where R represents the resistance.

$$t = C \times R \times \log(V) \tag{2}$$

Increased peak discharge voltage allows for increased instantaneous current discharge through the sample, resulting in higher overall power and heating rates. The non-monotonic correlation of capacitance density and discharge voltage with diameter was unexpected but may indicate a shift in mechanism. This has previously been observed in a partial dependence analysis of a machine learning guided FJH study that found that an increasing current density results in a shift from reaction-limited to diffusion-controlled kinetics.[40,41] This shift

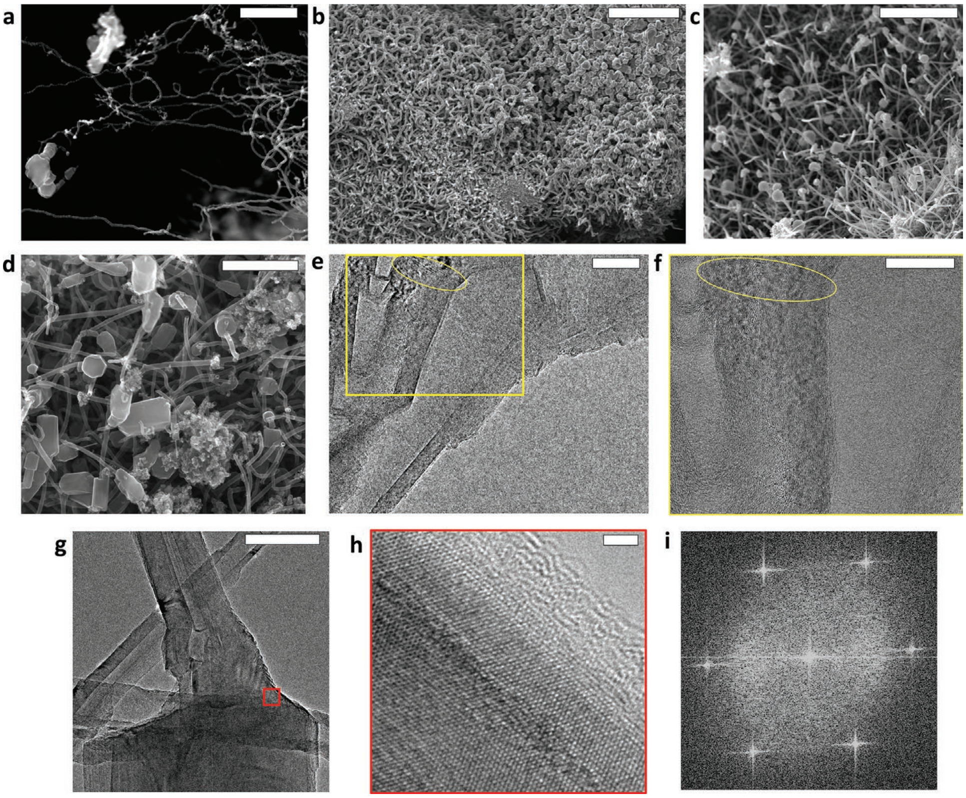

Figure 4. Electron microscopy images showing areas of 1D and 2D morphologies colocalizing to form graphitic hybrid materials and molecular dynamics models. a–d) SEM images showing colocalization and coalescence of 1D and 2D graphitic materials, with 2D morphologies attached to the ends of 1D morphologies. e) TEM image showing an area of colocalization of a bamboo-like carbon nanofibers with the edge of a graphene sheet. f) High-resolution TEM image of the area highlighted in (e). The circled area highlights the lattice fringe between the bamboo-like carbon nanofibers and graphene sheet, showing that they are part of the same crystal lattice. g) TEM image of a bamboo-like nanofiber merging with a graphene flake. h) Atomic-resolution bright-field TEM image of the area highlighted in (g) showing the hexagonal arrangement of carbon atoms in the graphene sheets uninterrupted at the junction between the 1D and 2D morphologies. i) Fast Fourier transform showing AB stacking in the hybrid material shown in (h). The scale bars in images correspond to: a) 20 µm, b,c) 3 µm, d) 1 µm, e,f) 20 nm, g) 100 nm, and h) 20 Å.

in growth kinetics is common in crystalline materials and may be observed here as well.[64,65] Representative SEM images of the F1DM as each parameter is varied are presented in Figures S14–S17, Supporting Information and demonstrate that the formation of F1DM is parameter sensitive, allowing for control of product morphologies.

Qualitative analysis also indicates that catalyst type, loading, capacitance density, and discharge voltage can be used to control the morphological makeup of F1DM (Figure 5e–h). Use of Ni(II) results in the highest share of 2D materials while Co(II) yields the most hybrid materials. As the catalyst loading decreases, the amount of hybrid and 1D morphologies produced also decreases, likely due to a lower density of catalytic sites for mobile carbon deposition (Figure 5f). As power input to the system increases, through applied voltage or capacitance density, the amount of 1D and hybrid materials increases. The diameter of the F1DM product is positively correlated to the amount of hybrid morphology present. Optimized reaction parameters yield 68% of the 1D/hybrid morphology (Figure 5i). Iterative mixing or sieving was used to further increase the yield of F1DM up to 90% (Figures S18 and S19, Supporting Information).

As the catalyst is loaded on or in the plastic, and the conductive CB reaches lower temperatures due to a lack of high-resistance junctions, we hypothesized that only the polymer feedstock forms the F1DM morphology, while the conductive additive forms 2D morphologies. The conductive additive is essential to the FJH process to reduce the resistance of the sample and allow for high power discharge. To increase the yield of the 1D morphology, iterative mixing is used, where the F1DM product (50/50 1D and 2D morphologies) is used as the conductive additive in a second FJH reaction, increasing the 1D share to ≈75%, without degradation in quality. Use of a larger grain conductive additive, such as metallurgical coke, allows the use of simple sieving to separate the small F1DM product from the large grain conductive additive. Sieving or iterative mixing allows for the production of F1DM that is composed of 80–90% 1D and hybrid morphologies without using solvent- or centrifugation-based separation methods.

3. Discussion

3.1. Mechanism of F1DM Formation

Catalyst-loaded conductive additive does not result in the formation of F1DM, but rather 2D graphene morphologies surface

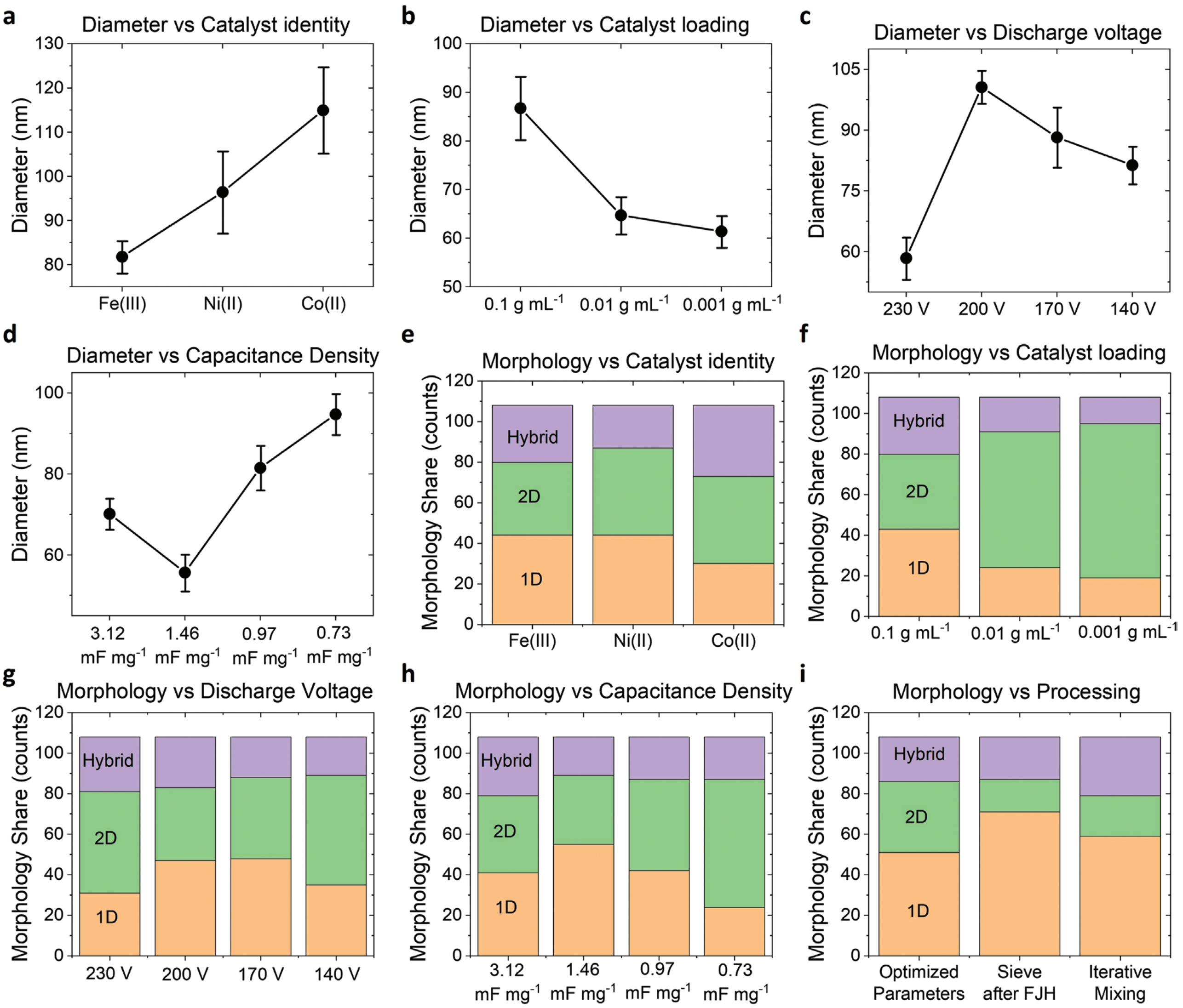

Figure 5. Quantitative analysis of size and morphology control through FJH parameter tuning. a–d) Confidence interval plots examining the effect that catalyst species (a), catalyst concentration in the wetting solution (b), peak voltage during FJH (c), and capacitance density applied during FJH (d) has on the diameter of the F1DM, as determined by SEM images. The mean diameter is shown by the dot, with a 95% confidence interval shown by the error bars. A line connecting the mean of each sample is provided to guide the eye. Stacked column plots examining the effect that e) catalyst species, f) catalyst concentration in the wetting solution, g) discharge voltage applied during FJH, and h) capacitance density applied during FJH has on the morphology of the F1DM, as determined by SEM images. i) Examining the morphological composition of the sample used in the vinyl ester composites; the sample obtained after sieving; and the sample obtained from iterative mixing twice. Each data point in (a–d) represents 120 individual carbon nanofibers or nanotubes, from 6 randomly selected areas of the sample to ensure an accurate average was obtained. In (e–i), 108 randomly selected areas for each sample (12 images, each divided into 9 equal area regions) were imaged and assigned a dominant morphology, either 1D, 2D, or hybrid. The optimized parameters to maximize 1D and hybrid morphology share is 0.1 g mL^{-1} of Fe(III), with discharge of 200 V and capacitance density of 1.46 mF mg^{-1}.

decorated with metal nanoparticles (Figure S20, Supporting Information). High resistance junctions and volatile decomposition imparted by the plastic feedstock are essential for the formation of F1DM. We hypothesized that these junctions form hot spots which facilitate F1DM nucleation. To further study this effect, a homogeneous sample with similar overall resistance and density was studied. Ash resulting from the industrial pyrolysis of plastic waste has a similar 7 Ω resistance to the carbon-added F1DM feedstock but is homogeneous. Surface wetting was used to introduce metal salt to the pyrolysis ash, and the sample was subjected to FJH using the same parameters used to form F1DM. No 1D morphologies were observed by SEM and TEM imaging (Figure S21a, Supporting Information) suggesting that resistive junctions at the plastic surface are required to form 1D morphologies.

To further probe if the resistive junctions are indeed a mechanistic cause of the F1DM formation, the process was replicated using sand (silica) rather than plastic. All parameters, including surface wetting the sand to introduce the catalyst, mixing with carbon black conductive additive, and FJH settings, remained identical. The sample was ground after FJH and sieved to remove the residual inert silica. The results (Figure S21b, Supporting Information) showed graphitization of the carbon black, as well as minor SiC formation, with <20 area% of the carbon being converted to F1DM, while the remainder was converted to 2D graphene morphologies. This experiment demonstrates that the resistive junctions are indeed necessary for the formation of F1DM, but also indicates that the carbon from the plastic is important for large amounts of F1DM to be produced. Recent work has shown that carbonization in the presence of carbon black or other conductive amorphous carbons can result in the metal catalyst free formation of turbostratic carbon nanoparticles.[29] Amorphous carbon can be converted to graphene sheets as the minor side products in CNT formation.[26] This further supports our observation that the 2D graphene sheets are produced from the carbon black.

TEM images show the presence of metallic nanoparticles at the base of plastic derived F1DM (Figure S22a, Supporting Information). The lattice spacing matches that of the metal oxide of the original catalyst used, suggesting that during the FJH process, the high temperatures result in degradation of the metal salt to form nanoparticles that facilitate deposition of mobile carbon which then nucleate to form the thermodynamically favored graphitic domains that elongate into F1DM. At lower catalyst loading concentrations, fewer or smaller nanoparticles will form, and 2D graphene morphologies will form, explaining why F1DM morphology and diameter vary with catalyst concentration. Similarly, the type of salt catalyst will determine the degradation temperature at which catalytic nanoparticles will form, and the rate of nanoparticle formation, impacting F1DM formation. Both metal nanoparticles and metal oxide nanoparticles are known to catalyze the growth of CNF and CNT materials, so it is unknown if the nanoparticles formed in situ during the FJH reaction are metal or metal oxide. It is likely that the catalytically active species are the neutral metal species, which are then converted to oxide once the sample is removed from the FJH reactor and exposed to air. Since the metal or metal oxide catalyst nanoparticles are formed in situ during the FJH reaction, there is no need to add expensive catalysts such as noble metal nanoparticles to the reaction scheme, as are often used in CVD methods. To better understand the relationship between catalyst concentration and F1DM diameter, TEM imaging was used to probe the size of the catalytic nanoparticles as catalyst concentration changed. Figure S22b, Supporting Information shows that when the catalyst loading concentration is decreased, the size of the catalytic nanoparticles decreases, which results in a decrease in the diameter of F1DM. At high metal salt loadings, some catalytic nanoparticles can be seen without a surrounding F1DM coating. This indicates that the catalyst concentration in the wetting solution has control over the size and abundance of nanoparticles formed.

The catalytic effect of Fe, Ni, and Co particles in synthesis of carbon 1D structures is commonly considered in CVD conditions, where carbon-containing feedstock is deposited on the nanoparticle's surface, diffuses through the particle, and is incorporated into the growing graphitic domain.[66] The majority of previous studies were focused on carbon nanotube formation from gaseous sources, leaving catalytic graphitization of amorphous carbon unexplored.[67] Previous work has demonstrated that stopping the FJH reaction early results in a carbonized product with substantial amorphous content, and considerable graphitic lattice disorder, suggesting an amorphous intermediate between polymer and graphitic product.[36] Further, since a mixture of morphologies is obtained, rather than only 1D morphologies as is commonly obtained from the catalytic pyrolysis of plastics, this suggests that a different mechanism may be occurring. The solid amorphous intermediate can be converted to graphitic products, which are 1D when on the catalytic nanoparticles. To investigate the effect of metal inclusions within the FJH setup, we examined the behavior of the amorphous carbon domain in contact with the Ni nanoparticle (**Figure 6**a) through molecular dynamics simulations. The system was heated and kept at 3000 K for 4 ns to simulate high temperatures of FJH. The amorphous carbon undergoes thermal and catalytic graphitization, both accelerated due to high FJH temperatures. Catalytic graphitization involves dissolution of carbon atoms, both from amorphous and already partially graphitized domains, into the Ni particle which then deposits on the surface, forming large 1D or hybrid graphitic domains (Figure 6b). The large size of the catalytic nanoparticle (450 Ni atoms) resulted in a large diameter carbon product distinct from existing literature results.[68] Analyzing the graphitization rate, we determine that the catalytic process accelerates amorphous carbon conversion (Figure 6c,d) and the curvature and size of the metallic nanoparticles favor the formation of 1D and hybrid morphologies.

3.2. Utility in Vinyl Ester Nanocomposites

Due to high tensile strengths, thermal and electric conductivities, and low densities, both 1D and 2D graphitic morphologies show promise in composites. Hybrid materials are hypothesized to result in excellent mechanical properties due to the 2D morphology increasing interfacial attachment between nanomaterial and matrix. The F1DM are highly dispersible in a 1% Pluronic surfactant aqueous medium allowing concentrations of 1.63 mg mL^{-1}(Figure S23, Supporting Information).

F1DM reinforced vinyl ester resin nanocomposites tested using nanoindentation demonstrated a dramatic increase in compressive modulus at even 0.5 wt% resulting in a 21% increase (Figures S24 and S25, Supporting Information). Macro-scale mechanical testing indicates substantial improvements under tensile extension and compression (**Figure 7**a,b, Figures S24 and S25, Supporting Information) with the F1DM composites showing 92%, 130%, and 48% increases in tensile strength and 174%, 304%, and 63% increases in toughness at 0.5, 2, and 5 wt%, respectively. The decrease in mechanical properties as the loading is increased from 2% to 5% is likely a result of F1DM aggregation in the vinyl ester matrix material. It is well known that nanocomposites do not exhibit a linear increase in mechanical properties as more reinforcing agent is added, but rather have an optimal maximum, usually less than 5% loading.[69,70] The interphase properties of polymer nanocomposites are complex and directly impact the macroscale mechanical properties, but can depend on surface area, aspect ratio, and dispersibility of nanomaterials, viscosity of the matrix material, and interfacial interactions between the phases.[71,72] F1DM loaded vinyl ester was compared with the composite

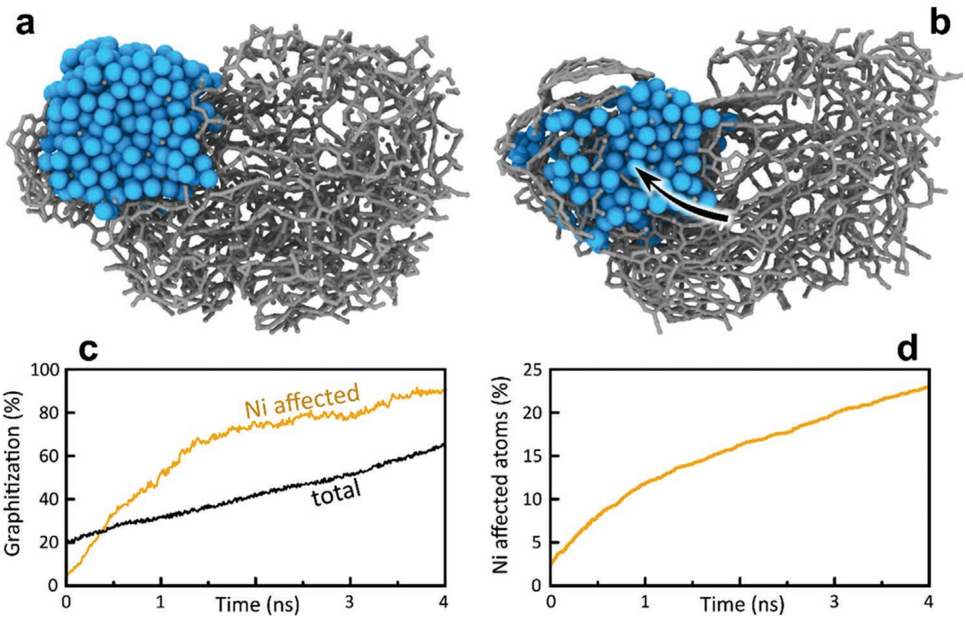

Figure 6. Atomistic simulations of the amorphous carbon (gray) annealed at 3000 K in contact with a Ni nanoparticle (blue). a) Configuration after initial pre-annealing already shows some carbon atoms dissolved within the metal particle, while b) the final structure shows the beginning of the carbon fiber formation through carbon interaction and catalytic graphitization, as indicated by the arrow. c) Graphitization level of all carbon (black) and carbon affected by Ni, indicating the catalytic effect that the Ni atoms have on the graphitization of affected carbon atoms. d) The percentage of carbon affected by Ni particle throughout the simulation indicating interaction of the mobile carbon with the Ni catalyst even in the short simulated timescale.

properties of vinyl ester loaded with commercially available carbon nanotubes made using traditional methods (Figure 7a). F1DM outperforms commercial nanotubes tested in nanoindentation and macro-scale compressive testing (Figure 7a), likely due to the hybrid morphology and high graphitic purity, and F1DM improves the properties of neat vinyl ester matrix material (Figure 7b). To demonstrate the advantage of F1DM as compared to graphene produced by FJH without the inclusion of catalysts, we compared the best-performing sample (5% F1DM) with a similarly prepared sample that contains 5% 2D graphene produced by FJH. The data is included in Figure S24, Supporting Information and demonstrates that F1DM outperforms graphene produced by FJH in nanoindentation testing. This is likely due to the hybrid morphology of F1DM improving matrix penetration and strain propagation properties of the vinyl ester. Thus, it is demonstrated that the F1DM hybrid morphology mechanically outperforms both 1D and 2D graphitic carbon nanomaterials as an additive in vinyl ester.

1D graphitic nanomaterials are well-known for their conductivity, and this property is often capitalized upon in nanocomposite materials. As such, the conductivity of the produced F1DM/vinyl esters was measured (Figure S26, Supporting Information), which demonstrates an increase in conductivity as the loading increases; however, commercial MWCNT outperforms the F1DM as a conductive additive. This is likely a result of the longer aspect ratio of commercial MWCNT when compared to the F1DM.

3.3. Cradle-to-Gate Life Cycle Assessment

A cradle-to-gate life-cycle assessment was conducted to examine the FJH method of F1DM synthesis as the impacts of application and disposal will vary negligibly based on the synthetic method of the graphitic 1D material. The life-cycle assessment scope, goal, functional unit, and inventory are included in the Experimental Section. A general scheme for the industrial synthesis of nanotubes and the life cycle inventories are shown in Scheme S1, Supporting Information. A full spreadsheet of values used is included in the Supplemental Information.

This life-cycle assessment considers two different synthetic scenarios: melt mixing of waste polymer and surface wetting of virgin polymer, further described in the Experimental Section, to determine the cumulative energy demand, global warming potential, and cumulative water use (Figure 7c–e). F1DM synthesis is compared to FJH 2D graphene synthesis from post-consumer waste plastic, where no catalyst loading is needed.[43] F1DM synthesis using surface wetting consumes 683 MJ and 185 L of water and produces 27 kg of CO_2 equivalent per kg of graphitic product produced. Most of the impacts result from the virgin polymer and conductive additive. When considering the melt mixing scenario, the process uses 395 MJ and 111 L of water, while producing 26 kg of CO_2 equivalent per kg of graphitic product produced. The impacts resulting from the synthesis of the waste polyethylene are disregarded, but the collection and separation burdens are considered. For the waste polymer melt mixing scenario, most burdens result from FJH.

Comparing the FJH synthesis of graphitic 1D and hybrid materials to literature is complicated by the wide variety of morphologies produced. Single-walled nanotubes are not considered a comparable product; only multiwalled nanotubes or nanofibers are compared. Comparing the FJH synthesis of F1DM to International Standards Organization compliant life-cycle assessments of graphitic 1D materials indicates a reduction in both energy use and global warming potential to

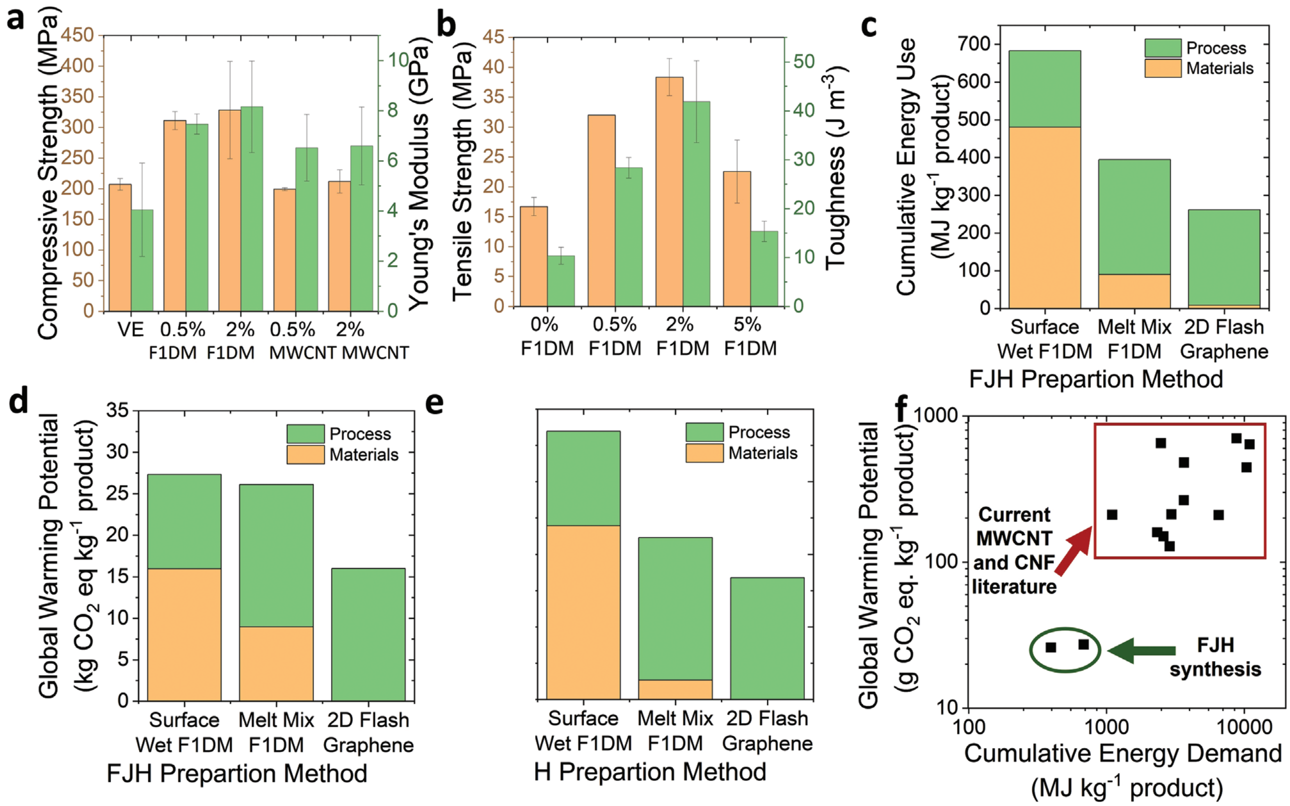

Figure 7. Quantitative comparison of F1DM utility in composites and sustainability with commercial alternatives. a,b) Mechanical analysis of vinyl ester nanocomposites reinforced with F1DM in bulk scale compressive testing as compared with commercial multiwalled carbon nanotubes (MWCNT) (a) and F1DM in tensile testing as compared to neat matrix material (b). c) Cumulative energy demand, d) global warming potential, e) cumulative water use associated with F1DM synthesis of F1DM through the surface wetting or melt mixing catalyst loading strategy, as compared to the FJH synthesis of 2D flash graphene where a metal catalyst is not required. f) A comparison of the two FJH synthesis of F1DM strategies considered in the life-cycle assessment, as compared with literature life-cycle assessment probing the synthesis of carbon nanotubes or nanofibers. The data presented in (f) is also presented in table form with references of the studies compared in Table S1, Supporting Information.

synthesize 1 kg of graphitic 1D material (Figure 7f; data also presented with references in Table S1, Supporting Information). The literature average for cradle-to-gate energy demand to form 1 kg of graphitic 1D materials is 4855 MJ, while the average global warming potential is 355 kg of CO_2 equivalent, representing 86–92% decrease in cumulative energy demand and a 92–94% decrease in global warming potential for the FJH route.

4. Conclusion

FJH can rapidly and controllably synthesize a variety of high value graphitic 1D or hybrid materials using earth-abundant simple salts and waste plastic, with demonstrated value, in an inexpensive, sustainable, and efficient manner. Analysis of the effects of these parameters contributes to an increased knowledge of the fundamental FJH mechanism. We anticipate that this framework can be expanded to form doped or functionalized F1DM.[56]

5. Experimental Section

Synthesis of F1DM: The F1DM were synthesized using a custom-built FJH reactor, as previously detailed and further discussed in the Supplemental Information. Specifically, the catalyst-loaded polymer feedstock can be prepared by surface wetting or melt mixing. For the surface wetting method: a solution of 80/20 v/v mixture of water and ethanol was prepared, with the salt of choice dissolved in the solution. For example, $FeCl_3$ at a concentration of 0.1 g mL^{-1} solution. Then, 5 g of <0.1 mm grain size virgin or waste polymer was submerged in the solution and sonicated for 15 min. The polymer with salt solution was vacuum filtered to remove excess salt solution. The polymer was dried overnight at room temperature to afford the catalyst-loaded polymer, which has a slight color change depending on the salt used. For the melt mixing method: ferrocene was selected as the catalyst due to its low melting point of 173 °C. The heater in the melt mixer was set to 175 °C, and a mixture of 4.95 g of HDPE and 0.05 g of ferrocene was melt-mixed to homogeneity using a Braebender 350-E heated zone melt mixer. The melt mix was then cooled to room temperature and ground to a fine powder using an electric hammer mill.

The catalyst-loaded polymer resulting from surface wetting or melt mixing was then mixed with the conductive additive. Amorphous carbon black (Cabot) was used for all samples in this manuscript, except when metallurgical coke was specified to have been used as a less expensive alternative. When amorphous carbon black was used as the conductive additive, 20 wt% was ground with 80 wt% of the catalyst-loaded polymer. Due to the small particle size of the amorphous carbon black, it coats the polymer homogeneously. Because of the higher cost of carbon black relative to waste plastic, an alternative feedstock of metallurgical coke, a coal-derived product that costs \$150 ton^{-1}, was also demonstrated effective (Figure S2, Supporting Information). Since metallurgical coke has a larger grain size of ≈150 µm, a higher weight percent must be used to achieve a similar final sample conductivity. For the use of metallurgical coke as the conductive additive, 40 wt% was used, and was mixed with 60 wt% of catalyst loaded polymer. Grain size of both the polymer and the conductive additive might impact the ratio of polymer feedstock and conductive additive. The conductive additive and polymer were mixed by hand, using a mortar and pestle. Then, 0.20 g of the homogeneous mixture was loaded into a quartz tube, with an internal diameter of 8 mm, with the sample compressed in tube by graphite electrodes to contain the powder. The sample can then be loaded into the FJH reactor, connecting the capacitors to be able to discharge through the resistive sample. An initial resistance of 6–8 Ω was used for the samples here. The sample was enclosed in a vacuum desiccator at ≈20 mmHg to facilitate outgassing of heteroatoms and volatiles (Figure S1, Supporting Information). A FJH current discharge pulse of the desired voltage, using the desired capacitance, was then discharged to completion through the sample, lasting 1–3 s, depending on the voltage and capacitance, with higher capacitance resulting in longer durations. The circuit was opened fully for 5 s, with a typical discharge only lasting 1–3 s. The voltage on the capacitors was fully discharged, which may require multiple discharges. A bright flash can be observed from the sample because of the black body radiation produced. See Figure S1, Supporting Information for extensive safety parameters and further considerations. After the FJH, the resistance of the sample decreases to 0.6–1 Ω. The F1DM was then emptied from the quartz tube, ground using a mortar and pestle, and characterized without further purification. The yield of F1DM ranges (40–60 wt% of reactant recovered as graphitic product) depending on the parameters, polymer type, grain size, and amount of conductive additive used.[36]

The remaining mass was converted to oils, waxes, and gases that distill and outgas during the FJH process. These volatiles have been preliminarily characterized in prior work, showing that waxes composed of oligomers of the parent polymers were produced with minimal oxidation.[36] These oils and waxes compose ≈10 wt% of the yield, and lighter hydrocarbons including methane and short-chain hydrocarbons, were produced. Large amounts of hydrogen were also known to be produced. These hydrocarbon products may have similar product distributions to flash pyrolysis processes. Further work is being carried out to characterize and quantify these volatile products. The volatiles can be readily trapped in gas sampling bags or vacuum cold traps, and thus removed from the voltage discharge, so there was no explosive hazard if the gases were vented or trapped away from the reaction. It was likely that upon product scale-up these volatiles would be recovered and used as another value stream or incinerated to power the F1DM production. Standard plastics pyrolysis methods that were industrialized worldwide capture the volatile streams and sell them into lubricants and fuel oil markets.[73]

To demonstrate that residual metal catalyst can be removed from the F1DM if necessary for a specific application, a sample of F1DM was soaked overnight in 1 M HCl, prior to vacuum filtration and rinsing with deionized water, however, this was not done for other samples. The standard parameters used to produce the materials characterized in Figure 1–3 were synthesized using a 0.1 g mL^{-1} surface wetting of iron(III) chloride, with a peak voltage of 170 V and a capacitance density of 0.97 mF mg^{-1}. A typical current versus time and temperature versus time graph is included in Figure S27, Supporting Information. Previous work has found high current FJH of carbon black and similarly conductive and high carbon content feedstocks produced 85–95% mass yield as only 2D graphitic morphologies.[40] However, when plastics were used as the starting material, although similar sheet-like and wrinkled 2D morphologies were obtained, the overall mass yield was substantially lower due to the volatile outgassing that occurs since the plastics were carbonized prior to graphitization taking place. ≈15–35% of the mass of starting material was recovered as graphitic product.[36,74] The yield of polymer-derived graphitic materials depends on the plastic identity, amount of atomic carbon in the feedstock, and FJH parameters.[36]

Dispersibility Testing and Vinyl Ester Composite Fabrication: F1DM was dispersed in a 1% surfactant aqueous solution using Pluronic-F127, a non-ionic polyol surfactant. Varying amounts of ground F1DM powder were weighed into centrifuge tubes, and solvent was added to yield the initial loading concentration (≈1 mg F1DM powder mL^{-1} of solvent). The centrifuge tubes were then sonicated in a cup-horn sonicator for 10 min (Cole-Parmer Qsonica 448) and centrifuged at 550 relative centrifugal force for 5 min to remove larger aggregates. The supernatant was decanted after centrifugation and diluted 100× since the graphene concentration leads to a very high absorbance. The absorbance of the solution was measured at 660 nm. The concentration was determined using Beer's Law with an extinction coefficient of 66 L g^{-1} cm^{-1}.

7 g of F1DM was produced to test loadings of 0.5, 2, and 5 wt%. The F1DM was readily dispersible in the vinyl ester matrix material through brief cup horn sonication. Vinylester (VE) resin was obtained from Fiberglass Supply Depot and used as received. Methyl ethyl ketone peroxide (MEKP) was obtained from Fiberglass Supply Depot and used as received as a catalyst/hardener for the resin. F1DM/VE Composites were prepared by combining 5.0 g of VE and 20–200 mg of F1DM, depending on the desired loading, in a 20 mL scintillation vial. The solution was then mixed using a magnetic stir bar for 30 min at 300 rpm. After stirring, the solution was then shear mixed with a homogenizer obtained from Cole-Parmer (Tissue Tearor 986370-07 Homogenizer; 120 VAC, 1.2 A) for 5 min at ≈10 000 rpm. 5 drops (≈0.15 g) of MEKP were then added to the solution while stirring with a magnetic stir bar at 300 rpm for 5 min. The solution was then poured into a PDMS mold coated with release agent and allowed to cure overnight.

Life-Cycle Assessment: A cradle-to-gate life-cycle assessment consists of a systematic analysis of the demands and impacts associated with a product from raw materials required for synthesis to the processing and manufacturing of the product and does not examine the final disposal end-use application or disposal of the product. The specific goal of this life-cycle assessment was to evaluate the demands and environmental impacts resulting from the FJH production of F1DM to compare with literature benchmarks studying the production of graphitic 1D materials synthesized using other methods. The system considered here covers three main steps: raw material production, reaction feedstock preparation, and FJH reaction. Transportation of raw materials was not considered here, and a lab-scale process was assumed. The functional unit considered here was 1 kg of high purity graphitic 1D material powder, with a >95% graphitic content, as this was the purity level commonly sold for gram-scale or larger applications, such as composites or coatings. The environmental impacts pertaining to the production of waste polyethylene were not considered in this study since it was a waste product and its demands or impacts were attributed to the primary use; however, the burdens for collection and separation of postconsumer waste polyethylene have been included.[75] Direct energy inputs for the FJH process were measured experimentally (Figure S27, Supporting Information), and cumulative demands and impacts were calculated using Argonne National Laboratory GREET life-cycle assessment.

The surface wetting method uses virgin HDPE powder, wet by 4 L of 80/20 v/v water/EtOH solution per kg of polymer, bath sonicated for 15 min, and centrifugation recovering 75% of the solution. The polymer mixture was air dried, and 20 wt% carbon black was mixed in using ball milling. The mixture of salt loaded polymer and conductive additive was then FJH and used without further purification, resulting in 1 kg of F1DM mixed morphologies that was >95% carbon and graphitic content. Alternatively, the melt mixing method considers waste polyethylene with iron acetylacetonate at a 0.25 wt% loading. The homogeneous melt mix was cooled and electrically hammer milled to 1 mm particle size, then mixed with 33 wt% metallurgical coke (3 mm particle size) to give a conductive mixture. The mixture was then FJH, pushed from the quartz tube, and sieved to separate the F1DM from the metallurgical coke, affording highly pure 1D morphologies with >95% carbon and graphitic content. Direct comparison of the life-cycle assessment with other literature values was possible if all databases utilized (e.g., GREET, SimaPro, Ecoinvent, and Gabi) follow International Standards Organization best standard procedures. Literature values presented in this discussion all comply with this requirement.

Computational Methods: Atomistic molecular dynamics simulations were performed on a system containing 450 Ni atoms and 4000 carbon atoms. Ni was selected as it was non-magnetic. The initial carbon configuration was generated by random positioning and misorientation of small graphitic flakes and randomly positioned individual carbon atoms (≈80% of the total carbon atoms). A small spherical area of the carbon structure was removed, and Ni particle was placed to form a substantial contact area. The initial configurations were pre-annealed at 800 K for 1×10^{-9} s to eliminate irregularities caused by the structure creation protocol, then heated to the target temperature of 3000 K with a heating speed of 0.5×10^{-12} K s^{-1} using a Nose–Hoover thermostat (canonical NVT ensemble) with a temperature damping parameter of 0.025×10^{-12} s. The structures were held at the target annealing temperatures for 4×10^{-9} s. Atomic interactions were represented by ReaxFF potential[76] as implemented in the LAMMPS[77] package.

Characterization and Measurements: Raman spectra were collected using a Renishaw inVia Raman microscope outfitted with a 5 mW 532 nm laser, 5 mW 633 laser, and 5 mW 785 nm laser. A 50× objective lens was used to collect all spectra. Analysis of Raman spectra, including peak intensity ratios, utilize the height of the peak. Custom Python scripts were used to analyze Raman spectral mapping data. Briefly, spectra were smoothed using a Savitsky–Golay filter, background-corrected using a polynomial fit, and averaged to give bulk sample characteristics. The LiveTrack software was automatically used to adjust focus between spectra. If a G peak could not be identified within the collected spectrum, the spectrum was assumed to be poorly focused and was not employed in the analysis. This occurred <3% of the time. XPS data were collected using a PHI quantera SXM scanning X-ray microprobe with a base pressure of 5×10^{-9} Torr. Survey spectra were recorded using 0.5 eV step sizes with a pass energy of 140 eV. Elemental spectra were recorded using 0.1 eV step sizes with a pass energy of 26 eV. All the XPS spectra were corrected using the C1s peaks (284.6 eV) as reference. TGA thermograms were collected using a TA Instruments Q-600 Simultaneous TGA/differential scanning calorimeter (DSC) using alumina pans, with a heating rate of 5 °C min^{-1} up to 780 °C. Air atmosphere at a flow rate of 80 mL min^{-1} was used to purge the sample chamber. Powder XRD spectra were collected using a Rigaku SmartLab II using zero background sample holders at a scan rate of 1° min^{-1} and a 0.05° step size. SEM images were taken with an FEI Helios Nanolab 660 Dual Beam SEM System. A voltage of 15 keV was employed in imaging. TEM and SAED images were obtained on a JEOL 2100 field-emission transmission electron microscope at an acceleration voltage of 200 kV. Samples were prepared by drop-casting extremely dilute F1DM/ethanol solutions onto lacey carbon grids. ICP-MS was carried out using a Perkin Elmer Nexion 300 ICP-MS. A Braebender 350-E heated zone melt mixer was used to melt-mix the catalyst into the polymer.

Supporting Information

Supporting Information is available from the Wiley Online Library or from the author.

Acknowledgements

K.M.W. and J.T.L. contributed equally to this work. K.M.W. and J.L.B. would like to acknowledge the NSF Graduate Research Fellowship for generous funding. The authors thank the Air Force Office of Scientific Research (FA9550-22-1-0526) and the Army Corp of Engineers ERDC (W912HZ-21-2-0050) for their gracious support of the FJH and other research projects. K.V.B. and B.I.Y. additionally thank the Office of Naval Research (N00014-22-1-2788).

Conflict of Interest

A company has licensed the FJH approach for graphene synthesis from Rice University. J.M.T. is a stockholder in that company, but not an employee, officer, or director. Potential conflicts of interest are mitigated through regular disclosures to and compliance with Rice University's Office of Sponsored Programs and Research Compliance. The authors declare no other potential conflicts

Data Availability Statement

The data that support the findings of this study are available in the supplementary material of this article.

Keywords

carbon hybrid nanomaterials, flash Joule heating, life-cycle assessment, plastic upcycling

Received: October 18, 2022
Revised: January 18, 2023

[1] P. M. Ajayan, O. Z. Zhou, in *Carbon Nanotubes*, (Eds.: M. S. Dresselhaus, G. Dresselhaus, P. Avouris), Springer, Berlin/Heidelberg, Germany **2001**, pp. 391.
[2] S. Rathinavel, K. Priyadharshini, D. Panda, *Mater. Sci. Eng., B* **2021**, *268*, 115095.
[3] J. C. Ruiz-Cornejo, D. Sebastián, M. J. Lázaro, *Rev. Chem. Eng.* **2020**, *36*, 493.
[4] W. Yang, X. Liu, X. Yue, J. Jia, S. Guo, *J. Am. Chem. Soc.* **2015**, *137*, 1436.
[5] C. Shi, K. A. Owusu, X. Xu, T. Zhu, G. Zhang, W. Yang, L. Mai, *Small* **2019**, *15*, 1902348.
[6] L. Kou, Y. Liu, C. Zhang, L. Shao, Z. Tian, Z. Deng, C. Gao, *Nano-Micro Lett.* **2017**, *9*, 51.
[7] L. Feng, N. Xie, J. Zhong, *Materials* **2014**, *7*, 3919.
[8] Z. Jia, K. Kou, M. Qin, H. Wu, F. Puleo, L. F. Liotta, *Catalysts* **2017**, *7*, 256.
[9] F. Liu, Y. Cheng, J. Tan, J. Li, H. Cheng, H. Hu, C. Du, S. Zhao, Y. Yan, M. Liu, *Front. Chem.* **2021**, *9*, 668336.
[10] Z. Wang, S. Wu, J. Wang, A. Yu, G. Wei, *Nanomaterials* **2019**, *9*, 1045.
[11] J. Restivo, O. S. Gonçalves Pinto Soares, M. F. Ribeiro Pereira, *Processes* **2020**, *8*, 1329.
[12] S. Kumar, G. Saeed, L. Zhu, K. N. Hui, N. H. Kim, J. H. Lee, *Chem. Eng. J.* **2021**, *403*, 126352.
[13] R. Kour, S. Arya, S.-J. Young, V. Gupta, P. Bandhoria, A. Khosla, *J. Electrochem. Soc.* **2020**, *167*, 037555.
[14] N. Wu, Q. Hu, R. Wei, X. Mai, N. Naik, D. Pan, Z. Guo, Z. Shi, *Carbon* **2021**, *176*, 88.
[15] Q. Xu, W. Li, L. Ding, W. Yang, H. Xiao, W.-J. Ong, *Nanoscale* **2019**, *11*, 1475.
[16] S.-H. Lee, J. Park, J. H. Park, D.-M. Lee, A. Lee, S. Y. Moon, S. Y. Lee, H. S. Jeong, S. M. Kim, *Carbon* **2021**, *173*, 901.
[17] B. McLean, E. I. Kauppinen, A. J. Page, *J. Appl. Phys.* **2021**, *129*, 044302.
[18] R. Rao, C. L. Pint, A. E. Islam, R. S. Weatherup, S. Hofmann, E. R. Meshot, F. Wu, C. Zhou, N. Dee, P. B. Amama, J. Carpena-Nuñez, W. Shi, D. L. Plata, E. S. Penev, B. I. Yakobson, P. B. Balbuena, C. Bichara, D. N. Futaba, S. Noda, H. Shin, K. S. Kim, B. Simard, F. Mirri, M. Pasquali, F. Fornasiero, E. I. Kauppinen, M. Arnold, B. A. Cola, P. Nikolaev, S. Arepalli, et al., *ACS Nano* **2018**, *12*, 11756.
[19] L. Yaqoob, T. Noor, N. Iqbal, *ACS Omega* **2022**, *7*, 13403.
[20] J. Wang, B. Shen, M. Lan, D. Kang, C. Wu, *Catal. Today* **2020**, *351*, 50.

[21] P. T. Williams, *Waste Biomass Valorization* **2021**, *12*, 1.
[22] C. Zhuo, Y. A. Levendis, *J. Appl. Polym. Sci.* **2014**, *131*, 39931.
[23] S. S. Sharma, V. S. Batra, *J. Chem. Technol. Biotechnol.* **2020**, *95*, 11.
[24] Y. Wang, N. Cai, H. Yang, C. Wu, *ACS Sustainable Chem. Eng.* **2022**, *10*, 2204.
[25] A. Bazargan, G. McKay, *Chem. Eng. J.* **2012**, *195*, 377.
[26] J. Gong, J. Feng, J. Liu, R. Muhammad, X. Chen, Z. Jiang, E. Mijowska, X. Wen, T. Tang, *Ind. Eng. Chem. Res.* **2013**, *52*, 15578.
[27] X. Jie, W. Li, D. Slocombe, Y. Gao, I. Banerjee, S. Gonzalez-Cortes, B. Yao, H. AlMegren, S. Alshihri, J. Dilworth, J. Thomas, T. Xiao, P. Edwards, *Nat. Catal.* **2020**, *3*, 902.
[28] A. Ahamed, A. Veksha, K. Yin, P. Weerachanchai, A. Giannis, G. Lisak, *J. Hazard. Mater.* **2020**, *390*, 121449.
[29] M. Jia, H. Bai, N. Liu, L. Hao, P. He, Z. Fan, J. Liu, R. Niu, J. Gong, T. Tang, *Macromol. Rapid Commun.* **2022**, *43*, 2100835.
[30] N. Cai, X. Li, S. Xia, L. Sun, J. Hu, P. Bartocci, F. Fantozzi, P. T. Williams, H. Yang, H. Chen, *Energy Convers. Manage.* **2021**, *229*, 113794.
[31] D. X. Luong, K. V. Bets, W. A. Algozeeb, M. G. Stanford, C. Kittrell, W. Chen, R. V. Salvatierra, M. Ren, E. A. McHugh, P. A. Advincula, Z. Wang, M. Bhatt, H. Guo, V. Mancevski, R. Shahsavari, B. I. Yakobson, J. M. Tour, *Nature* **2020**, *577*, 647.
[32] K. M. Wyss, D. X. Luong, J. M. Tour, *Adv. Mater.* **2022**, *34*, 2106970.
[33] Y. Yao, K. K. Fu, S. Zhu, J. Dai, Y. Wang, G. Pastel, Y. Chen, T. Li, C. Wang, T. Li, L. Hu, *Nano Lett.* **2016**, *16*, 7282.
[34] B. Deng, Z. Wang, W. Chen, J. T. Li, D. X. Luong, R. A. Carter, G. Gao, B. I. Yakobson, Y. Zhao, J. M. Tour, *Nat. Commun.* **2022**, *13*, 262.
[35] Y. Guo, Y. Zou, C. Cheng, L. Wang, R. I. Made, R. Goei, K. W. Tan, S. Li, A. I. Y. Tok, *Sci. Rep.* **2022**, *12*, 2522.
[36] W. A. Algozeeb, P. E. Savas, D. X. Luong, W. Chen, C. Kittrell, M. Bhat, R. Shahsavari, J. M. Tour, *ACS Nano* **2020**, *14*, 15595.
[37] K. M. Wyss, J. L. Beckham, W. Chen, D. X. Luong, P. Hundi, S. Raghuraman, R. Shahsavari, J. M. Tour, *Carbon* **2021**, *174*, 430.
[38] P. A. Advincula, D. X. Luong, W. Chen, S. Raghuraman, R. Shahsavari, J. M. Tour, *Carbon* **2021**, *178*, 649.
[39] K. M. Wyss, Z. Wang, L. B. Alemany, C. Kittrell, J. M. Tour, *ACS Nano* **2021**, *15*, 10542.
[40] M. G. Stanford, K. V. Bets, D. X. Luong, P. A. Advincula, W. Chen, J. T. Li, Z. Wang, E. A. McHugh, W. A. Algozeeb, B. I. Yakobson, J. M. Tour, *ACS Nano* **2020**, *14*, 13691.
[41] J. L. Beckham, K. M. Wyss, Y. Xie, E. A. McHugh, J. T. Li, P. A. Advincula, W. Chen, J. Lin, J. M. Tour, *Adv. Mater.* **2022**, *34*, 2106506.
[42] H. Xie, K. Fu, C. Yang, Y. Yao, J. Rao, Y. Zhou, B. Liu, D. Kirsch, L. Hu, *Small Methods* **2018**, *2*, 1700371.
[43] K. M. Wyss, R. D. De Kleine, R. L. Couvreur, A. Kiziltas, D. F. Mielewski, J. M. Tour, *Commun. Eng.* **2022**, *1*, 1.
[44] D. V. Kosynkin, A. L. Higginbotham, A. Sinitskii, J. R. Lomeda, A. Dimiev, B. K. Price, J. M. Tour, *Nature* **2009**, *458*, 872.
[45] A. Koutsioukis, K. Spyrou, N. Chalmpes, D. Gournis, V. Georgakilas, *Nanomaterials* **2022**, *12*, 447.
[46] A. C. Ferrari, D. M. Basko, *Nat. Nanotechnol.* **2013**, *8*, 235.
[47] A. Merlen, J. G. Buijnsters, C. Pardanaud, *Coatings* **2017**, *7*, 153.
[48] W. Chen, J. T. Li, Z. Wang, W. A. Algozeeb, D. X. Luong, C. Kittrell, E. A. McHugh, P. A. Advincula, K. M. Wyss, J. L. Beckham, M. G. Stanford, B. Jiang, J. M. Tour, *ACS Nano* **2021**, *15*, 11158.
[49] V. Carozo, C. M. Almeida, E. H. M. Ferreira, L. G. Cançado, C. A. Achete, A. Jorio, *Nano Lett.* **2011**, *11*, 4527.
[50] V. W. Brar, G. G. Samsonidze, M. S. Dresselhaus, G. Dresselhaus, R. Saito, A. K. Swan, M. S. Ünlü, B. B. Goldberg, A. G. Souza Filho, A. Jorio, *Phys. Rev. B* **2002**, *66*, 155418.
[51] D. K. Singh, P. K. Iyer, P. K. Giri, *Diamond Relat. Mater.* **2010**, *19*, 1281.
[52] B. Deng, D. X. Luong, Z. Wang, C. Kittrell, E. A. McHugh, J. M. Tour, *Nat. Commun.* **2021**, *12*, 5794.
[53] P. K. Tripathi, S. Durbach, N. J. Coville, *Nanomaterials* **2017**, *7*, 284.
[54] C. Wu, M. A. Nahil, N. Miskolczi, J. Huang, P. T. Williams, *Process Saf. Environ. Prot.* **2016**, *103*, 107.
[55] D. Yao, H. Li, B. C. Mohan, A. K. Prabhakar, Y. Dai, C.-H. Wang, *ACS Sustainable Chem. Eng.* **2022**, *10*, 1125.
[56] W. Chen, C. Ge, J. T. Li, J. L. Beckham, Z. Yuan, K. M. Wyss, P. A. Advincula, L. Eddy, C. Kittrell, J. Chen, D. X. Luong, R. A. Carter, J. M. Tour, *ACS Nano* **2022**, *16*, 6646.
[57] B. Vedhanarayanan, V. K. Praveen, G. Das, A. Ajayaghosh, *NPG Asia Mater.* **2018**, *10*, 107.
[58] Z. Yan, Z. Peng, G. Casillas, J. Lin, C. Xiang, H. Zhou, Y. Yang, G. Ruan, A.-R. O. Raji, E. L. G. Samuel, R. H. Hauge, M. J. Yacaman, J. M. Tour, *ACS Nano* **2014**, *8*, 5061.
[59] K. Xia, H. Zhan, Y. Gu, *Procedia IUTAM* **2017**, *21*, 94.
[60] M.-Q. Zhao, X.-F. Liu, Q. Zhang, G.-L. Tian, J.-Q. Huang, W. Zhu, F. Wei, *ACS Nano* **2012**, *6*, 10759.
[61] D. Yuan, L. Ding, H. Chu, Y. Feng, T. P. McNicholas, J. Liu, *Nano Lett.* **2008**, *8*, 2576.
[62] C. J. Thambiliyagodage, S. Ulrich, P. T. Araujo, M. G. Bakker, *Carbon* **2018**, *134*, 452.
[63] R. D. Hunter, J. Ramírez-Rico, Z. Schnepp, *J. Mater. Chem. A* **2022**, *10*, 4489.
[64] K. M. Carroll, A. W. Knoll, H. Wolf, U. Duerig, *Langmuir* **2018**, *34*, 73.
[65] R. Viswanatha, D. D. Sarma, in *Nanomaterials Chemistry: Recent Developments and New Directions*, (Eds: C. N. R. Rao, H. C. M. A. Müller, A. K. Cheetham), Wiley, New York **2007**, p. 139.
[66] M. Fouquet, B. C. Bayer, S. Esconjauregui, R. Blume, J. H. Warner, S. Hofmann, R. Schlögl, C. Thomsen, J. Robertson, *Phys. Rev. B* **2012**, *85*, 235411.
[67] B. Wang, C. H. P. Poa, L. Wei, L.-J. Li, Y. Yang, Y. Chen, *J. Am. Chem. Soc.* **2007**, *129*, 9014.
[68] W.-H. Chiang, R. M. Sankaran, *Nat. Mater.* **2009**, *8*, 882.
[69] R. O. Medupin, O. K. Abubakre, A. S. Abdulkareem, R. A. Muriana, A. S. Abdulrahman, *Sci. Rep.* **2019**, *9*, 20146.
[70] S. Roy, R. S. Petrova, S. Mitra, *Nanotechnol. Rev.* **2018**, *7*, 475.
[71] M. A. Ashraf, W. Peng, Y. Zare, K. Y. Rhee, *Nanoscale Res. Lett.* **2018**, *13*, 214.
[72] Y. Zare, *Composites, Part A* **2016**, *84*, 158.
[73] K. Jagodzińska, P. G. Jönsson, W. Yang, *Chem. Eng. J.* **2022**, *446*, 136808.
[74] K. M. Wyss, W. Chen, J. L. Beckham, P. E. Savas, J. M. Tour, *ACS Nano* **2022**, *16*, 7804.
[75] M. A. Martín-Lara, J. A. Moreno, G. Garcia-Garcia, S. Arjandas, M. Calero, *J. Cleaner Prod.* **2022**, *365*, 132625.
[76] J. E. Mueller, A. C. T. van Duin, W. A. Goddard, *J. Phys. Chem. C* **2010**, *114*, 4939.
[77] S. Plimpton, *J. Comput. Phys.* **1995**, *117*, 1.